Nanocrystallisation and self-assembly of biosourced ferulic acid derivative in polylactic acid elastomeric blends

Vikram Singh Raghuwanshi, Antoine Gallos, David Joram Mendoza, Maoqi Lin, Florent Allais, Gil Garnier

HAL Id: hal-03517349

https://agroparistech.hal.science/hal-03517349

Nanocrystallisation and Self-Assembly of Biosourced Ferulic Acid Derivative in Polylactic Acid Elastomeric Blends

Vikram Singh Raghuwanshi[*,1], Antoine Gallos[2], David Joram Mendoza[1], Maoqi Lin[1], Florent Allais[1,2], Gil Garnier[*,1,2]

[1] Bioresource Processing Research Institute of Australia (BioPRIA), Department of Chemical Engineering, Monash University, Clayton, Victoria-3800 Australia

[2] URD Agro-Biotechnologies Industrielles (ABI), CEBB, AgroParisTech, 51100 Pomacle, France

*Email: gil.garnier@monash.edu; vikram.raghuwanshi@monash.edu

Abstract

Hypothesis:

The crystallisation of biosourced ferulic acid derivatives - Bis-*O*-feruloyl-1,4-butanediol (BDF) - in a polylactic acid (PLA) produces thermoplastic elastomeric blends that are transparent and biodegradable. Elastomeric and transparency are controlled by the domain size. PLA-BDF blends up to a threshold BDF concentration providing elastomeric properties show no evidence of BDF crystallisation. Heat treatment weakens the PLA-BDF interaction, give BDF molecules mobility to interact with nearby BDF molecules, leading to BDF nano-crystallisation.

Experiments:

PLA-BDF blends were synthesised by hot-melt processing by mixing pure PLA with different concentrations of BDF (0-40 wt%) at 180 °C for 13 minutes. One set of blends was annealed at 50 °C for 24 h and compared with the unannealed set. The BDF crystallisation in the blends is studied by combining SAXS, SEM, XRD and Polarised Optical Microscopy. Monte-Carlo simulations were performed to validate SAXS data analysis.

Findings:

Unannealed PLA-BDF blends of up to the threshold of 20 wt% BDF are dominated by the semicrystalline behaviour of PLA, without any trace of BDF crystallisation. Surprisingly, the PLA-BDF 40 wt% blend shows BDF crystallisation in the form of large and nanoscale structures bonded together by weak interparticle interaction. At concentrations up to 20 wt%, the BDF molecules are homogenously dispersed and bonded with PLA. Increasing BDF to 40 wt% brings the BDF molecules close enough to crystallise at room temperature, as the BDF molecules are still bonded with the PLA network.

Annealing of PLA-BDF blends led to BDF nanocrystallisation and self-assembling in the PLA network. Both BDF nanoparticle size and interparticle distance decrease as the BDF concentration increases. However, the number density of BDF nanocrystals increases. The formed BDF nanocrystals have size ranging between 100 and 380 Å with interparticle distance of 120-180 Å. The structure factor and potential mean force confirm the strong interparticle interaction at the higher BDF concentration. Heat treatment weakens the PLA -BDF interaction, which provides mobility to the BDF molecules to change conformation and interact with the nearby BDF molecules, leading to BDF crystallisation. This novel BDF crystallisation and self-

assembly mechanism can be used to develop biodegradable shape memory PLA blends for biomedical, shape memory, packaging and energy applications.

Introduction

Polylactic acid (PLA) is a bio-based, degradable and easy to process polyester of good mechanical properties; it is a promising polymer to engineer applications in biomedical devices[1, 2], sensors[3] and energy [4] [5]. PLA is a semicrystalline thermoplastic polyester derived from corn, sugar beets and sugarcane[6] and sustains inherent properties of transparency, low-toxicity, biocompatibility and recyclability. PLA has been studied extensively and is widely used as an alternative to petroleum-based polymers in commercial applications such as food packaging[7], electronics[8], housewares, agriculture[9], automobile[10], drug delivery[11] and biomedical devices[12-14]. However, the PLA based technologies remain limited due to its high cost, poor thermal stability and plastic mechanical properties (hard and brittle). Thus, a necessity has emerged to overcome PLA drawbacks and develop novel materials for advance manufacturing. Here, blending PLA with other materials has played a preponderant role.

Different strategies of copolymerisation, modifying by plasticizers and other polymer additives have been developed to overcome PLA drawbacks[15, 16]. These strategies bring flexibility and ductility to PLA-based materials. In particular, plasticizers and toughening agents such as polyethylene glycol (PEG)[17, 18], triethyl citrate (TEC)[19], poly(ester-urethane)[20], and acetyl tributyl citrate (ATBC) [21, 22], poly(ether-b-amide) elastomeric copolymer (PEBA)[23], poly(butylene adipate-co-terephthalate) (PBAT)[24], glucosemonoesters and thermoplastic starch (TPS)[25] are used to improve PLA-blend properties [26]. It was reported that the melt elasticity and viscosity increase as increases the poly (epichlorohydrin-co-ethylene oxide) copolymers (ECO) content in PLA blends [27]. Blending 20 wt% ECO in PLA increases the elongation at break from 5% to 160%. Blending PLA with a plasticizer also reduces the glass transition temperature (T_g)[28]. However, the blending plasticizers/additives must have good miscibility and be homogenously distributed within the PLA network. Poor miscibility of plasticizers leads to phase separation and crystallisation which usually render the blend hard and brittle. For sustainability, another important consideration while blending is that the additive retains the composability and renewability properties of PLA; very few do.

Recently, a novel family of bio-sourced additives made from Bis-*O*-feruloyl-1,4-butanediol (BDF) - was developed to homogenously blend with PLA[29]. Interestingly, BDF added shape memory (SM) and ductility properties to the PLA-BDF blend while retaining its transparency at room temperature. The PLA-BDF blends remember their original shape even after recovering from an important strain (400 %). The BDF-PLA blend properties were observed to be significantly affected by the crystallisation of BDF molecules, phase separation and interaction with the PLA network. In particular, beyond a critical concentration (20 wt%), BDF molecules crystallise in PLA, leading to a phase separation which renders the blend opaque and brittle. The relationship between BDF crystallisation, nanoscale structure and molecular interactions with the PLA network all determine the blend properties. Previous article reveals the BDF crystals formed due to the pi-pi interaction at the molecular level. However, the shape, size distribution and inter particle interactions of fully formed nanoscale crystals were not been explored. The effect of BDF crystallisation and its interaction with the PLA network on the

blend properties remain unknown and challenging to characterise. A fundamental understanding of BDF crystallisation in PLA is required at the nanoscale to efficiently design materials of desirable properties. The effect of BDF crystallisation and its interaction with the PLA network on the blend properties remain unknown and challenging to characterise. A fundamental understanding of BDF crystallisation in PLA is required to efficiently design materials of desirable properties.

In this study, a powerful method- small angle X-ray scattering (SAXS) - combined with X-ray diffraction (XRD), scanning electron microscopy (SEM) and polarised optical microscopy (POM), is applied to quantify crystallisation, self-assembly and to better understand the interaction mechanisms of BDF with the PLA network. The combination of these methods reveals key information on BDF crystallisation and assembly from the atomic to the nano and micrometer scales. Original (unannealed) and annealed (at 50 °C for 24 h) PLA-BDF blends of BDF concentration ranging from 10 to 40 wt% are studied. The processes of crystallisation and self-assembly of BDF upon heat treatment are quantified by determining the BDF morphology, size distribution and interparticle interactions. SEM and POM visualise the large and nanosized structures. This work contributes to both the fundamental and engineering aspects for developing novel PLA based materials able to replace the current non-biodegradable materials for biotechnologies and advanced applications.

Materials and Experiment:

Materials

The PLA was purchased from NatureWorks (Ingeo™ 4043D) and used without purification. The molecular weight is 70,000 g/mol. The average density of PLA is 1.21-1.25 g/cm^3 and the monomer size ($C_3H_4O_2$) of PLA is about 3.7 Å (0.37 nm) [A]. The chemical structure of the PLA is given in Fig 1(a). The Bis-*O*-feruloyl-1,4-butanediol (BDF) was synthesised at URD ABI, AgroParisTech, France. Details on the BDF preparation were described elsewhere [29]. The chemical composition of BDF is $C_{24}H_{30}O_8$ and the molecular weight is 446.50 g/mol. The size of BDF in open conformation is 25 Å (2.5 nm). The chemical structure of BDF is given in Fig 1(b).
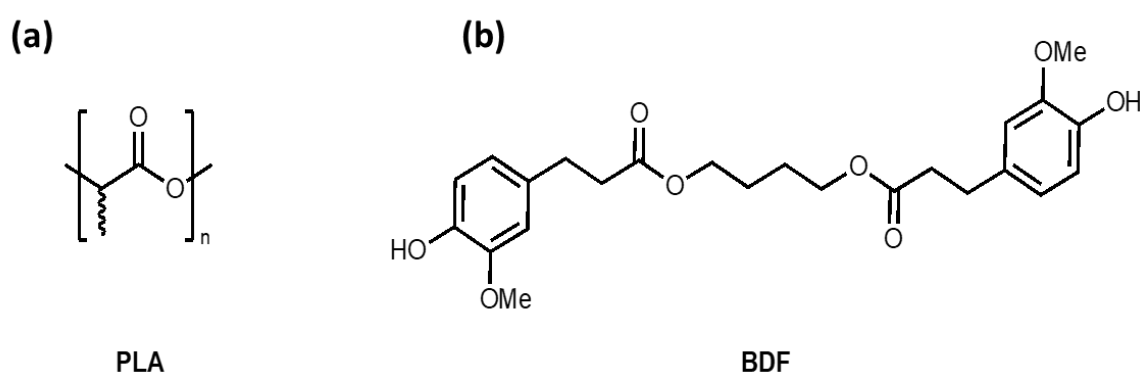

(a) PLA

(b) BDF

Figure 1: (a) Monomer unit of lactic acid. (b) Monomer unit of Bis-O-feruloyl-1,4-butanediol (BDF)

PLA-BDF blend preparation

The PLA-BDF blends were synthesised by hot-melt processing using an internal mixer Haake Rheomix (Thermo Fisher Scientific) set at 50 RPM speed. The processing occurs at fixed temperature of 180 °C. Pure PLA was first incorporated and mixed for 2 minutes, then the

biosourced additives (BDF) were added and blended for 13 minutes. Two sets of samples were prepared with different concentration of BDF in the PLA network. (i) The unannealed PLA and PLA-BDF (10-40 wt%) blends, (ii) The PLA and PLA-BDF (10-40 wt%)) blends annealed at 50 °C for 24 h. The unannealed PLA sample is transparent. However, the unannealed PLA sample with high BDF amount 40 wt% and heat-treated PLA-BDF (>10 wt%) are white and opaque (Fig 2).
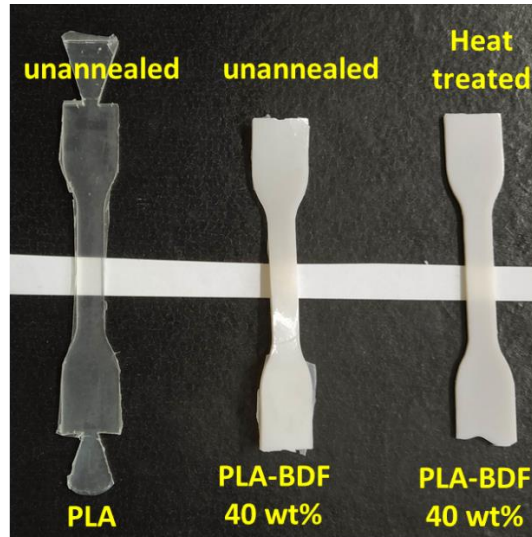

Figure 2: Images of the original (unannealed) transparent PLA (left); PLA blended with 40 wt% BDF (mid); and heat-treated PLA-BDF 40 wt% blend at 50 °C for 24 h (right).

Polarised optical microscopy (POM)
POM measurements were performed using a Nikon microscope (Nikon Eclipse Ni-E Model, Japan) equipped with polarised lens accessories. The measurements were made using the 100x lens magnification at the room temperature.

Scanning Electron Microscopy (SEM)
A FEI Magellan 400 FEGSEM was used for imaging PLA and PLA-BDF blend dog bones at the room temperature. The samples were coated with iridium (<1 nm) to avoid charging effects during SEM measurements.

X-ray diffraction (XRD)
X-ray diffraction (XRD) was performed using a Bruker D8 Advance diffractometer with Cu-Kα radiation, in the 2θ-range from 7 to 60° with a step size of 0.02° at the room temperature. Crystallographic properties of the pattern were analysed by the Pawley method (TOPAS 4.2)[30] to determine the space group and cell parameters.

Small angle X-ray Scattering (SAXS)
Small angle X-ray Scattering (SAXS) measurements were performed on all unannealed and heat-treated samples at the SAXS/WAXS beamline of the Australian Synchrotron [31]. Samples were measured in the transmission mode by using the X-rays of energy 15 KeV at the room temperature. The scatted X-rays from the sample were collected on the Pilatus detector which was placed at 7 m away from the sample position. The raw data was corrected for the dead time, transmission and air background by the inhouse software ScatterBrain. Finally, the scattering images were radially averaged and converted into 1D scattering curves. The SAXS curves were plotted as the scattering intensity against the scattering vector q which is related with the scattering angle and the wavelength of X-ray by $q = 4\pi\sin(\theta)/\lambda$ where θ is the scattering

4

angle and λ is the incident wavelength. The *q* values were calibrated by using the standard silver behenate. The pre-calibrated glassy carbon was used to the normalised the scattering intensity to the absolute values of scattering cross section. The SAXS curves where also simulated by the Monte-Carlo (MC) simulation using the package McSAS [32].

Results

The microstructures of unannealed and annealed (heat-treated) PLA and PLA-BDF blends are studied by polarised optical microscopy (POM). Fig. 3 shows the POM images of unannealed PLA (NC_1), PLA-BDF 20 wt% (NC_20) and PLA-BDF 40 wt% (NC_40) samples; these are compared to the homologous set of blends heat-treated at 50 °C for 24 h. The heat-treated blends are designated as PLA (C_1), PLA-BDF 20 wt% (C_20) and PLA-BDF 40 wt% (C_40) (C stands for crystalline). The unannealed PLA and PLA-BDF blends show no large-scale structures. The heat-treated C_1 without BDF exhibits no microstructures formation, while the PLA-BDF blends C_20 and C_40 clearly show the presence of large structures. The structures formed upon heat-treatment indicate phase separation in the blend.
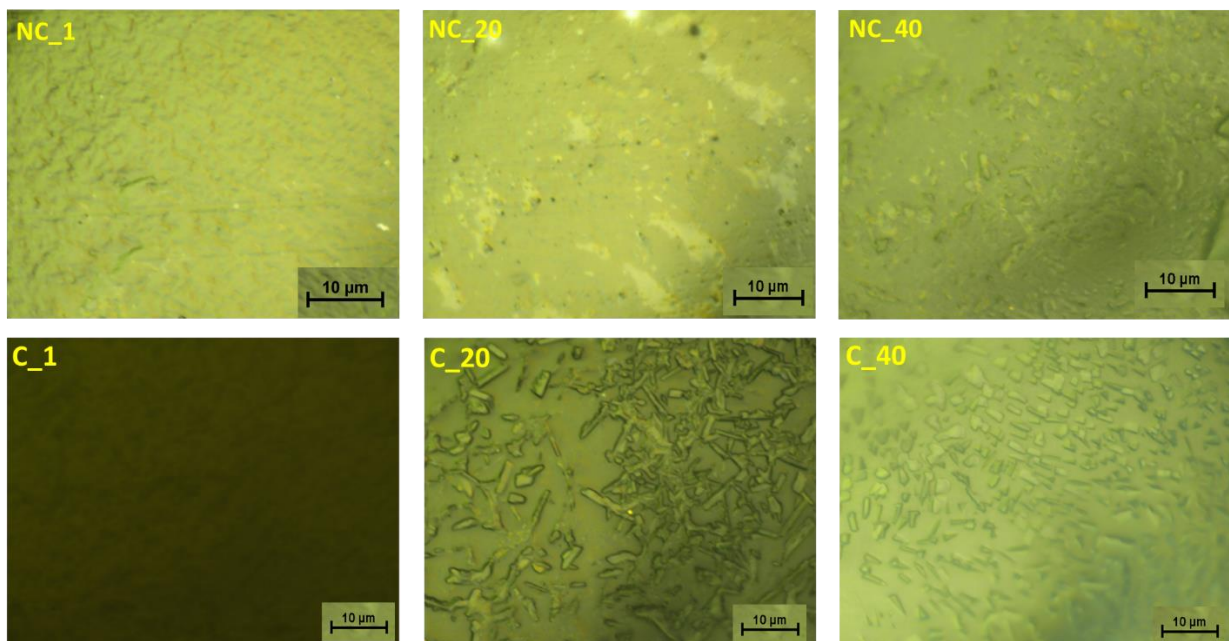

Figure 3: Polarised optical microscope (POM) images of the unannealed PLA (NC_1), PLA-BDF 20 wt% (NC_20) and PLA-BDF 40 wt% (NC_40). The bottom row shows the POM images of the heat-treated (annealed) homologous series: pure PLA (C_1) and PLA-BDF 20 wt% (C_20) and PLA-BDF 40 wt% (C_40). The samples were heat treated at 50 °C for 24 h. The scale bar represents 10 µm.

Scanning electron microscopy (SEM) is performed to provide better resolution of the structures at the nanoscale. The SEM micrograph of NC_1 shows the absence of nanostructures with only a fibre like structure observed (Fig 4), which might be from the PLA distribution. Surprisingly, the unannealed NC_40 blend clearly shows large separated nanostructure phases, unexpected without heat treatment. These nanostructures are random in shape, forming rods, cubes and spheres, and with a large particle size distribution between 100-300 nm. The SEM micrographs of the heat-treated C_20 and C_40 blends reveal the formation of large structures; this is as expected. The nanostructures in the C_20 blend is smaller (100-300 nm) compared to the microstructures in the C_40 blend with size ranging between 1 and 5 micrometres (Fig 4). These structures are also of random shape and large size distribution. Both POM and SEM

methods provide localised information over a small area and structures within depth of a few micrometres. Moreover, these techniques do not elucidate whether these structures are crystalline or amorphous.
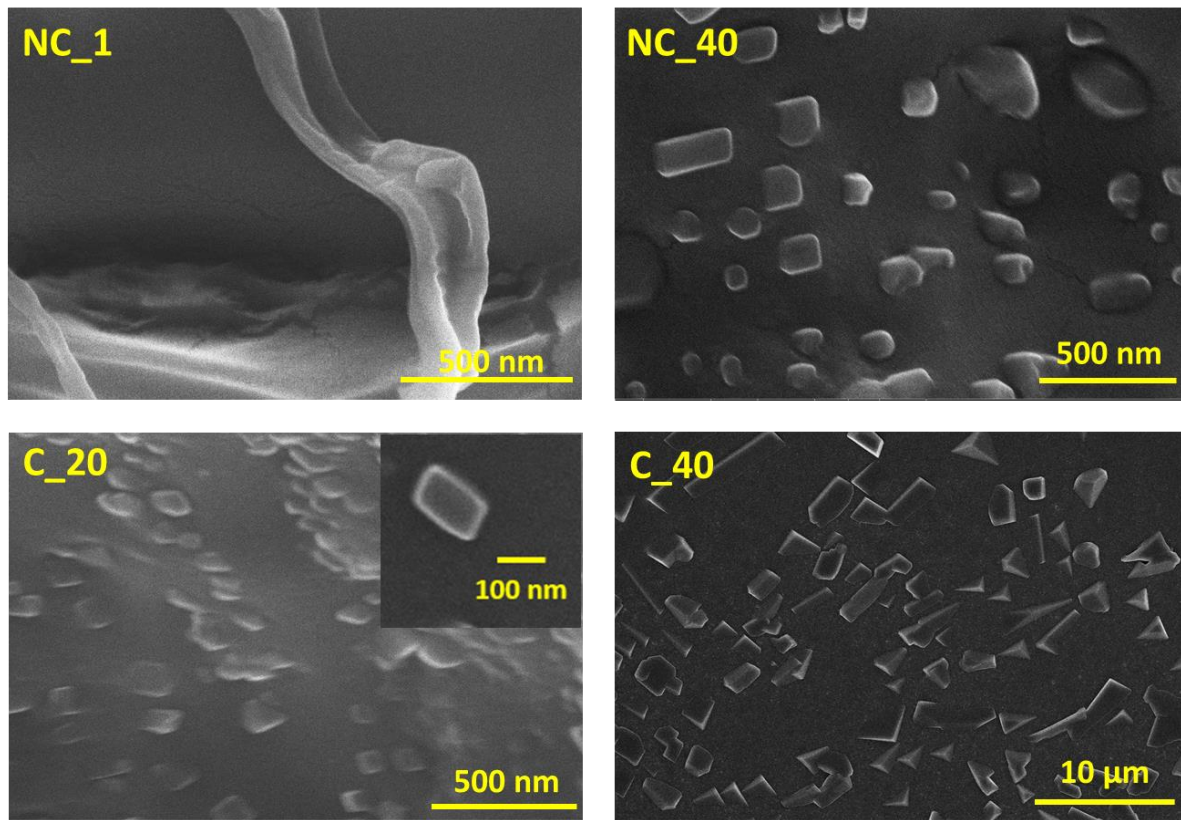

Figure 4: Scanning electron micrographs (SEM) of the unannealed PLA (NC_1) and PLA-BDF 40 wt% (NC_40). The bottom row shows the SEM of heat-treated PLA-BDF 20 wt% (C_20) and PLA-BDF 40 wt% (C_40). The samples were heat treated at 50 °C for 24 h.

A complementary and in-depth information over the complete volume of the blend is extracted from X-ray diffraction (XRD) and small angle X-ray scattering (SAXS) experiments. XRD provides structural characterization at the atomic scale and determines the phase composition of the elementary structure unit. Furthermore, XRD distinguishes between the crystalline and amorphous phases present in the blend [33]. However, it is difficult to characterize the nanostructure morphology, distribution, interaction and assembly mechanisms at the nanoscale using XRD. This is achieved by SAXS, a powerful analytical method which measures the lower 2θ angles and provides nanostructure formation and interaction information at the 1-100 nm size range [34-36].

XRD of the unannealed PLA and PLA-BDF blends up to 30 wt% BDF are dominated by the sharp semi crystalline peak of PLA at 2θ = 16.9° (Fig 5a). There is no evidence of BDF crystallisation peaks in these blends. However, the unannealed PLA-BDF 40 wt% blend shows multiple BDF crystallisation peaks indicating crystallisation in the blend without any heat treatment. The result is unexpected. However, it confirms that the structures observed by SEM are crystalline. Upon heat treatment, pure PLA shows a consistent semicrystalline XRD peak similar to the unannealed PLA (Fig 5b). However, on heat treatment, the amorphous region of the unannealed PLA in the XRD decreases (Supporting information, S3). The result indicates annealing of pure PLA reduces the amorphous region and increases the crystallinity in the sample. The crystallinity index of 23% is calculated for the pure PLA, which increase to 36% for the heat-treated PLA. Heating the PLA_BDF 10 wt% blend shows a minor peak originated

6

at $2\theta = 19.5°$ from the crystalline BDF phase. This peak confirms BDF crystallisation. XRD of heat-treated PLA-BDF blends of 20 wt% and higher shows pronounced BDF crystalline peaks at different 2θ positions, confirming the formation of BDF crystalline phase (Fig 5b). The blend also reveals a higher degree of crystallinity index of 65%.
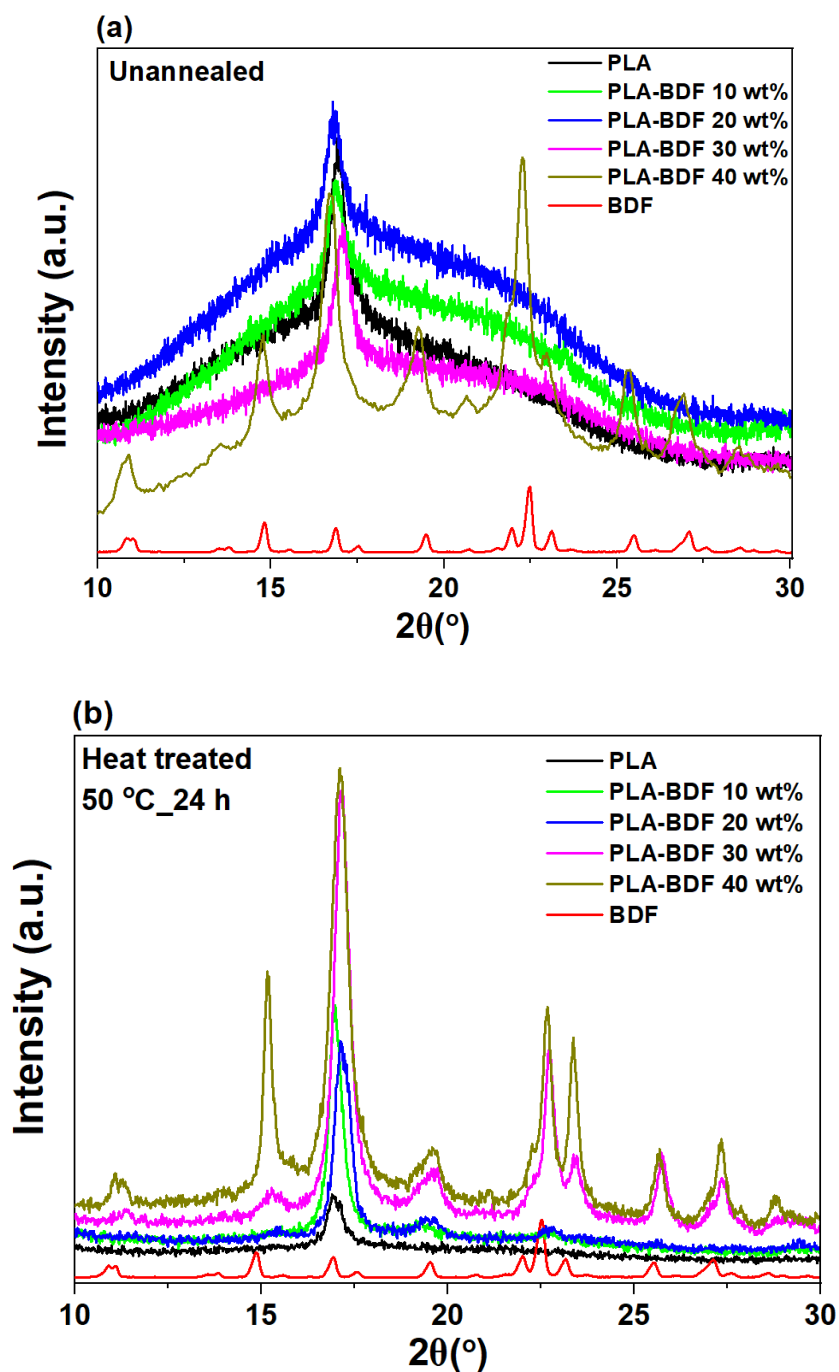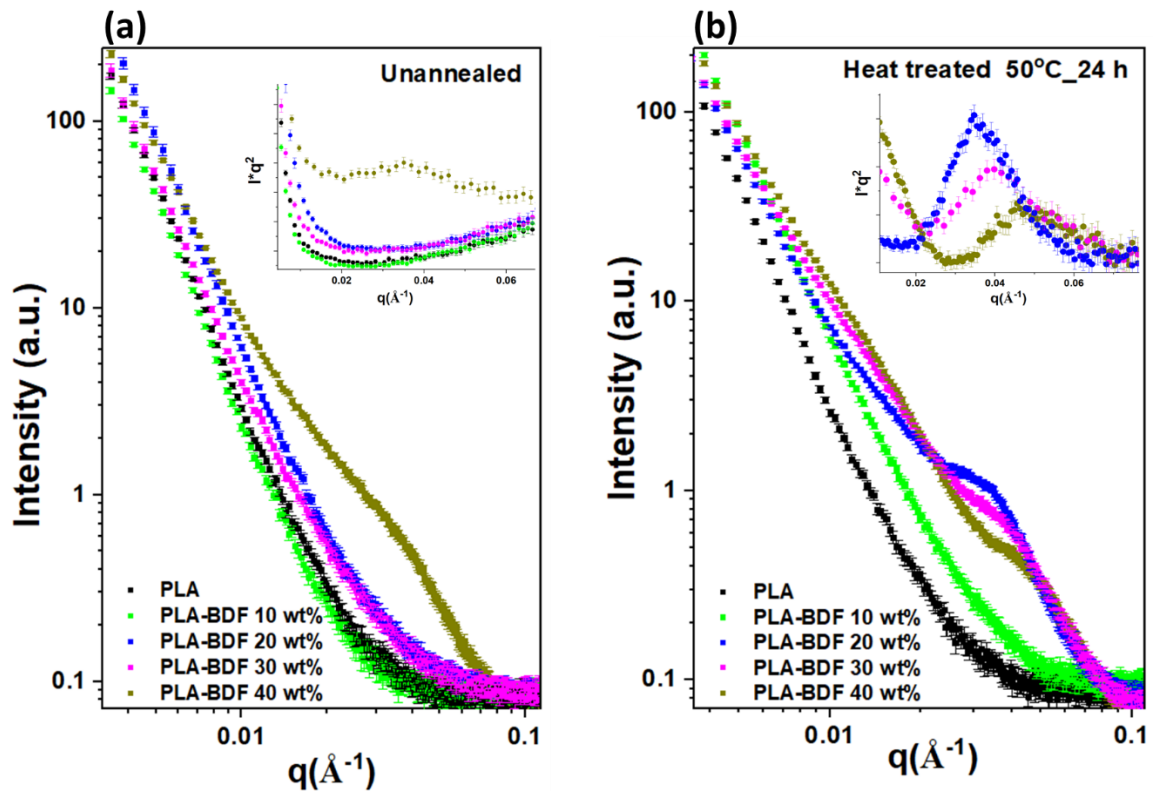

Figure 5: X-ray diffraction (XRD) of (a) unannealed PLA and PLA blended with different BDF concentration varying from 10-40 wt%. (b) XRD of the heat-treated PLA and PLA-BDF blends with different BDF concentrations. The samples were heat-treated at 50 °C for 24 h.

SAXS experiments were conducted to reveal the BDF nano-crystallisation and self-assembly mechanisms in PLA. The scattering images show isotropic scattering for all original and heat-treated PLA and PLA-BDF blends (Supporting information: S1), indicating random distribution

of nanostructures without any orientation. The radial averaging of scattering images provides 1D SAXS curves which are plots of scattering intensity as a function of the scattering vector q (Fig 6a, 6b), where q is defined as $q = 4\pi\sin\theta/\lambda$ with θ, the scattering angle and λ the X-rays wavelength.

The SAXS curves of unannealed PLA and PLA-BDF blends (up to 30 wt%) show no correlation peaks in their profile (Fig 6a). The upturn in the SAXS curves at $q < 0.01$ Å^{-1} follows the power law slope of q^{-4} which indicates the presence of larger structures from the PLA semicrystalline phase. The SAXS curve of the original PLA-BDF 40 wt % blend clearly shows a correlation peak centred at q=0.0345 Å^{-1}. This correlation peak indicates the assembly of nanostructures. The clarity of the peak is better seen from the Kratky plot of the SAXS curves presented in the inset of Fig 6a. The correlation peak position allows evaluating the centre to centre interparticle distance of 182 Å (18 nm) by the relation $d=2\pi/q$, where q is the correlation peak position. The upturn at the q values $q< 0.0345$ Å^{-1} comes from the large-scale structures which are beyond the scale of SAXS measurements. However, these large structures are clearly seen in the POM and SEM images.
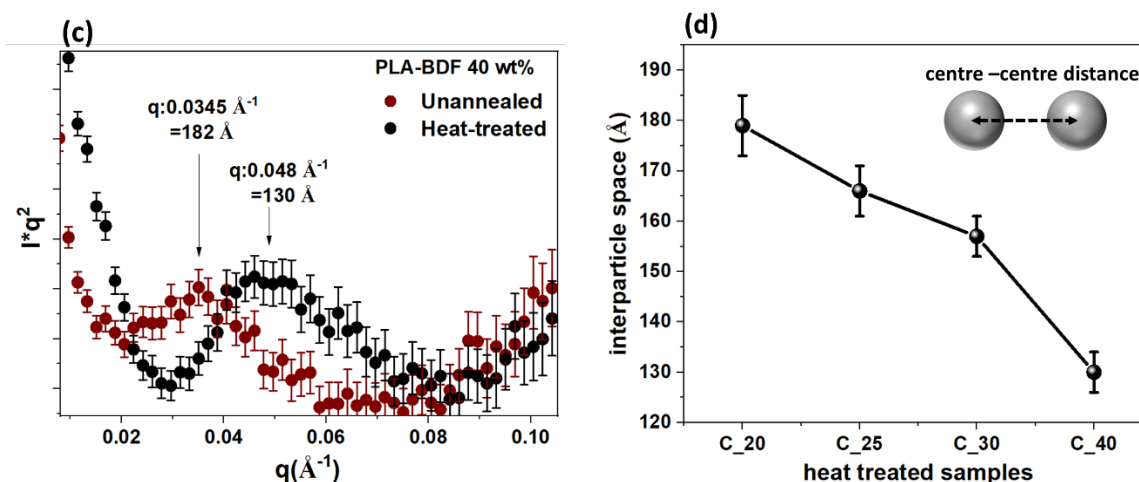
Figure 6: Small angle X-ray Scattering (SAXS) curves of: (a) unannealed PLA and PLA blended with different dosage of BDF ranging from 0-40 wt%. Inset showed the Kratky plot of the SAXS curves. (b) SAXS of the heat-treated PLA and PLA blended with different BDF concentrations. The samples were heat-treated at 50 °C for 24 h. Inset showed the Kratky plot of the SAXS curves. (c) Kratky plot of the SAXS curves of the unannealed and heat-treated PLA-BDF 40 wt% samples; (d) Interparticle distance of heat-treated PLA blended with BDF 20, 25, 30 and 40 wt%.

The SAXS curves of the heat-treated PLA and PLA-BDF 10 wt% blend show no correlation peak and the scattering is dominated by the large PLA semicrystalline structures (Fig 6b). The heat-treated PLA-BDF blends with 20 wt% BDF and higher clearly indicate the assembly of nanostructures by the presence of a correlation peak. Again, this correlation peak is visualised with the Kratky plot of the SAXS curves (inset Fig 6b). For the PLA-BDF 20 wt% blend, the correlation peak is at q = 0.035 $Å^{-1}$ which corresponds to a 179 Å interparticle spacing. The correlation peak shift towards higher q value of q= 0.048 $Å^{-1}$ for the PLA-BDF 40 wt% blend reveals a lower interparticle spacing of 130 Å (Fig 6b). It is worth noting that the interparticle distance for the heat-treated PLA-BDF 40 wt% blend is 1.4 times smaller than that of the unannealed PLA-BDF 40 wt% blend (182 Å, Fig 6d). The Kratky plot from Fig 6c shows the shift in the correlation peak for both blends.

Further information from the SAXS curves is extracted by fitting the form factor of a sphere combined with the log normal distribution of particles in the equation provided in the supporting information (S2). A sphere shape is assumed because it covers an average size of all shape particles and their interactions. To determine the interparticle interaction, a structure factor of hard spheres with the local monodisperse approximation is considered with the form factor. Only the SAXS curves for the blends with a correlation peak were fitted. For the Monte-Carlo simulations (MC) The SAXS curves were simulated by considering a sphere shape model of radius between 1-100 nm which retrieve model size distribution parameters from the scattering pattern. Details on the MC simulation and procedure are reported previously [B, C]. The size distribution resulting from SAXS curve fitting and MC are compared in Fig 7.

The heat-treated PLA-BDF 20 wt% blend shows a single particle size of 116 Å. For the same SAXS curve, MC simulation shows a bimodal distribution of particles of diameter 115 Å and 390 Å. The size of both small and large particles is decreasing as increases the BDF concentration in the blend. The heat-treated PLA-BDF 40 wt% have the smallest particles (96

Å) and large particle of diameter 280-290 Å. As a comparison, the original/unannealed PLA-BDF 40 wt% blend shows a single particle size of 117 Å (by simulation) or 110 Å (by fitting).
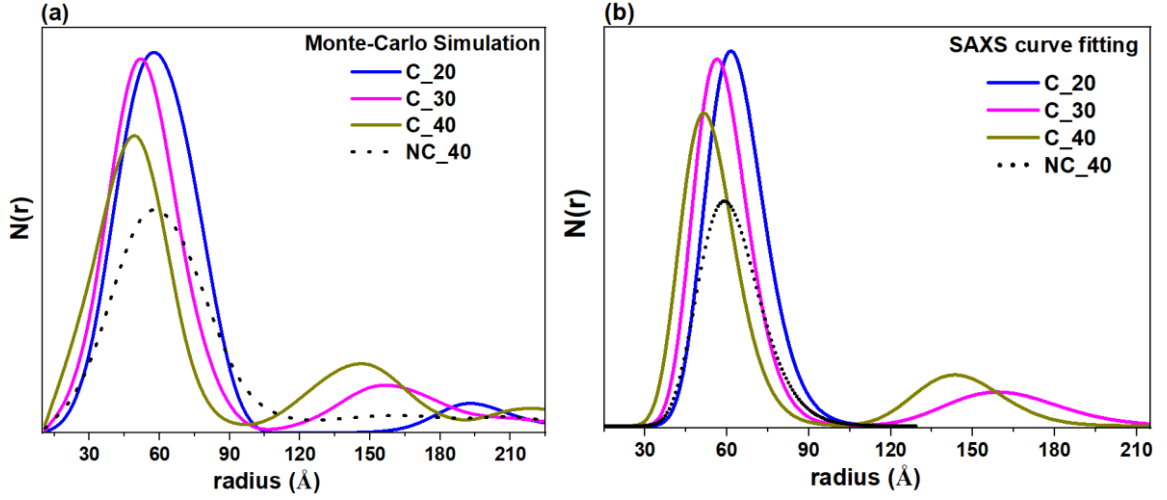

Figure 7: Size distribution from unannealed PLA with 40 wt% BDF and heat-treated PLA blended with different BDF concentrations (20 - 40 wt%). (a) Size distribution calculated by Monte Carlo simulation; (b) Size distribution obtained from SAXS curve fitting.

The interparticle interaction between the BDF nanostructures in the PLA network is determined by the structure factor (S(q)) from SAXS curves fitting. Fig 8a shows the S(q) of the unannealed PLA-BDF 40 wt% and heat-treated PLA-BDF blends with 20 wt%, 30 wt% and 40 wt% BDF. The S(q) for unannealed PLA-BDF 40 wt% shows a broad peak (grey dashed curve) indicating weak interparticle interaction. However, the heat-treated PLA-BDF 20 wt% has a sharp peak (blue solid line) indicating stronger interaction than the unannealed PLA-BDF 40 wt%. As increases the BDF concentration in the heat-treated blends, the S(q) peak becomes sharper and shifts towards higher q values, indicating an increase in the interparticle interactions.

The radial distance distribution G(r) is also evaluated from the S(q) by using the equation:

$$G(r) = 1 + \frac{1}{2\pi^2 r} \int_{qmin}^{qmax} q.(S(q) - 1).\sin(q.r)\, dq \qquad (1)$$

The peak positions in G(r) indicate the nearest neighbouring nanoparticles' distances in different surrounding shells (Fig 8b). The first peak in G(r) reveals nearest neighbouring particles in the 1st shell and the following peaks show nanoparticles in the 2nd and following shells. The heat-treated PLA-BDF 20 wt% blend has a single G(r) peak revealing the BDF particles are only present in the 1st surrounding shell with an interparticle spacing of 186 Å. However, the heat-treated PLA-BDF 40 wt% blend shows two peaks where the first peak indicates the nearest neighbouring first shell interparticle distance of 123 Å and the second peak of 285 Å revealing the 2nd shell neighbouring particles distance. This means the particles are arranged in a short-range order up to 300 Å and a long-range disorder beyond 300 Å. The maxima in the S(q) and G(r) at different BDF concentrations is caused by the interference effects from neighbouring particles. Moreover, the decay at the higher q and r values indicates the nanoparticles to be arranged in a self-assemble short-range order. An increase in the BDF concentration leads to an increase in the ordering of the BDF particles due to strong interactions.

The potential mean force (φ) indicates the average work required to bring two particles close to each other at a minimum distance of r. The minimum in the φ obtained at a particular r value reveals the nearest distance between two selected individual particles at the minimum energy of the system. The φ(r) is evaluated from the G(r) using the relation [37]:

$$\varphi(r) = -\mathrm{KT} \ln G(r) \qquad (2)$$

Rearranging equation 2 gives:

$$\varphi(r)/\mathrm{KT} = \ln(1/G(r)) \qquad (3)$$

where K is the Boltzmann constant and T is temperature. Figure 8c shows φ(r)/KT for the unannealed PLA-BDF 40 wt% and heat-treated PLA-BDF blend with 20 wt% and higher BDF concentration. The original PLA-BDF 40 wt% shows a shallow peak with the minima close to 180 Å. The shallowness of the peak indicates weak interparticle interaction as compared to the heat-treated samples. The φ(r) peak value for higher BDF concentration for PLA-BDF 40 wt% blend has a large minimum value of -2 with a smaller distance of 123 Å and strong interparticle interactions. The result signifies that at higher BDF concentration, the BDF nanoparticles come much closer to each other due to strong interactions.

The number density is calculated from SAXS curve fitting of the unannealed PLA-BDF 40 wt% and heat-treated sample PLA-BDF blends of different BDF content (20-40 wt%) (Fig 8d). The number density of the heat-treated PLA-BDF 20 wt% is 2.5×10^{16} particles/cm^3 which increases by 1.4 times (3.5×10^{16} particles/cm^3) for the heat-treated PLA-BDF 40 wt% blend. This means the particle number density increases as increases BDF upon heat treatment. However, the unannealed PLA-BDF 40 wt% blend shows a particle number density of 1.3×10^{16} particles/cm^3; this is 2.7 times smaller than for the heat-treated blend.
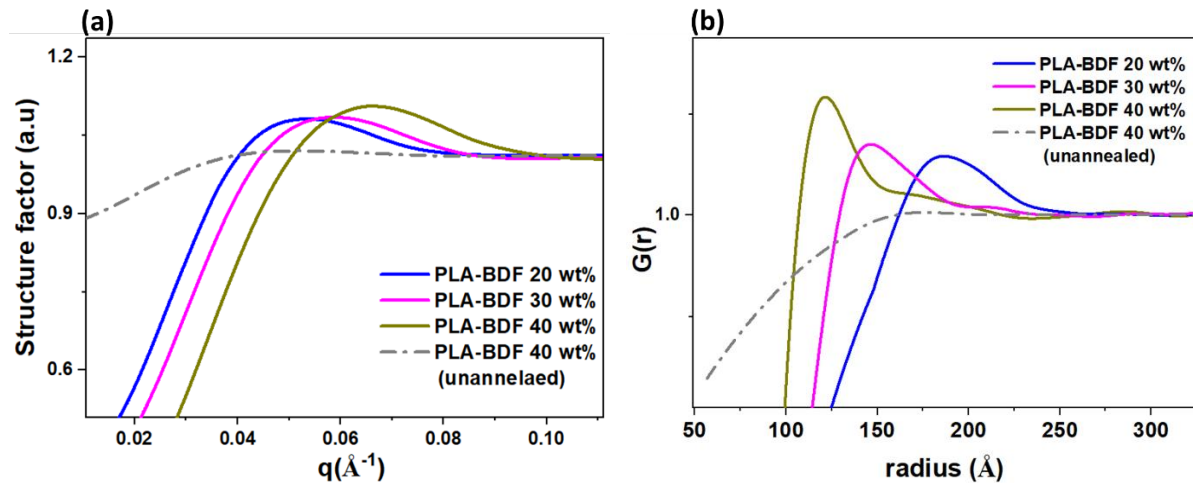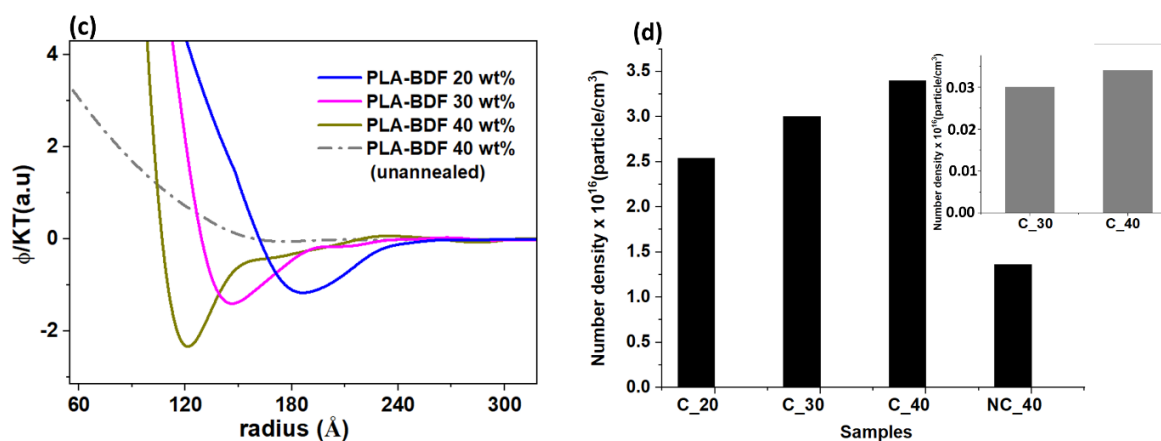
Figure 8: (a) Structure factor, (b) Radial distance distribution, (c) Potential mean force and (d) number density all extracted from the SAXS curves fitting for the unannealed PLA with 40 wt% BDF and heat-treated PLA blended with different BDF concentrations (20 -40 wt%).

Discussion

The mechanism of nanocrystallisation of the bio-sourced BDF additive in a PLA network is explored by combining SAXS, XRD, SEM and POM. BDF concentration and crystallisation have significant effects on the optical and mechanical properties of the PLA-BDF blend. The unannealed and heat-treated PLA and PLA-BDF blends- with up to 20 wt% BDF- are transparent, while higher BDF concentrations and heat treatment render the blend opaque (Fig 2). Transparency is due to the incident visible light directly passing through the material without any interaction or scattering. However, crystallisation of BDF in the blend forms large BDF structures, of nanometer and micrometer size, which scatter the incident visible light multiple times to make the blend opaque. The large BDF structures are clearly seen by POM, SEM and scattered X-rays in the lower q region of the SAXS curves.

In the unannealed PLA-BDF blends up to the threshold BDF concentration of 20 wt%, the BDF molecules remain well dispersed in the PLA network (Fig 9c). These BDF molecules are bonded with the PLA and do not have the sufficient energy to interact with neighbour BDF molecules to crystallise. XRD, SEM and POM do not show any evidence of BDF crystallisation and phase separation. However, at the higher BDF concentration of 40 wt% in PLA blends, XRD confirms the unexpected BDF crystallisation and SEM micrographs reveal the formation of large structures in the blend. A correlation peak in SAXS also confirms the nanoscale self-assembly of BDF nanocrystals with a size of 117 Å and interparticle distance of 182 Å.

An explanation for this unexpected BDF crystallisation is that at the higher BDF concentrations, the BDF molecules are much closer to each other in the blend. The low T_g of the blend allows the nearby BDF molecules to interact slowly and with time (aging), form crystalline phases. Still, these crystals remain linked with the PLA network which constrains their interaction with other nearly BDF crystals (Fig 9d). This results in the large interparticle distance and weak interparticle interactions measured between the BDF nanostructures in the PLA blend, as revealed by the broad peak of S(q) and G(r), and shallow peak in the φ analysis. Further analysis is required to fully elucidate the high BDF concentration dependent crystallisation for the unannealed PLA-BDF blends.

Heat-treatment of PLA-BDF blends with BDF content of 20 wt% and higher confirms the BDF crystallisation measured from the XRD patterns. The heat-treated PLA-BDF 40 wt% blend reveals smaller particle size (96 Å) and interparticle particle distance (130 Å) compared to the other blends. Upon heat treatment, the BDF molecules gain the sufficient energy to break

bonds with the PLA network, change conformation (shrink) and interact with nearby BDF molecules to crystallise (Fig 9e, 9f). More BDF molecules interact upon heating and form crystals. Thus, a higher number density of BDF crystals with smaller interparticle distance is observed, which have strong interparticle interactions and assembly; this is reflected by the sharpness of Sq and depth of φ/KT curves.
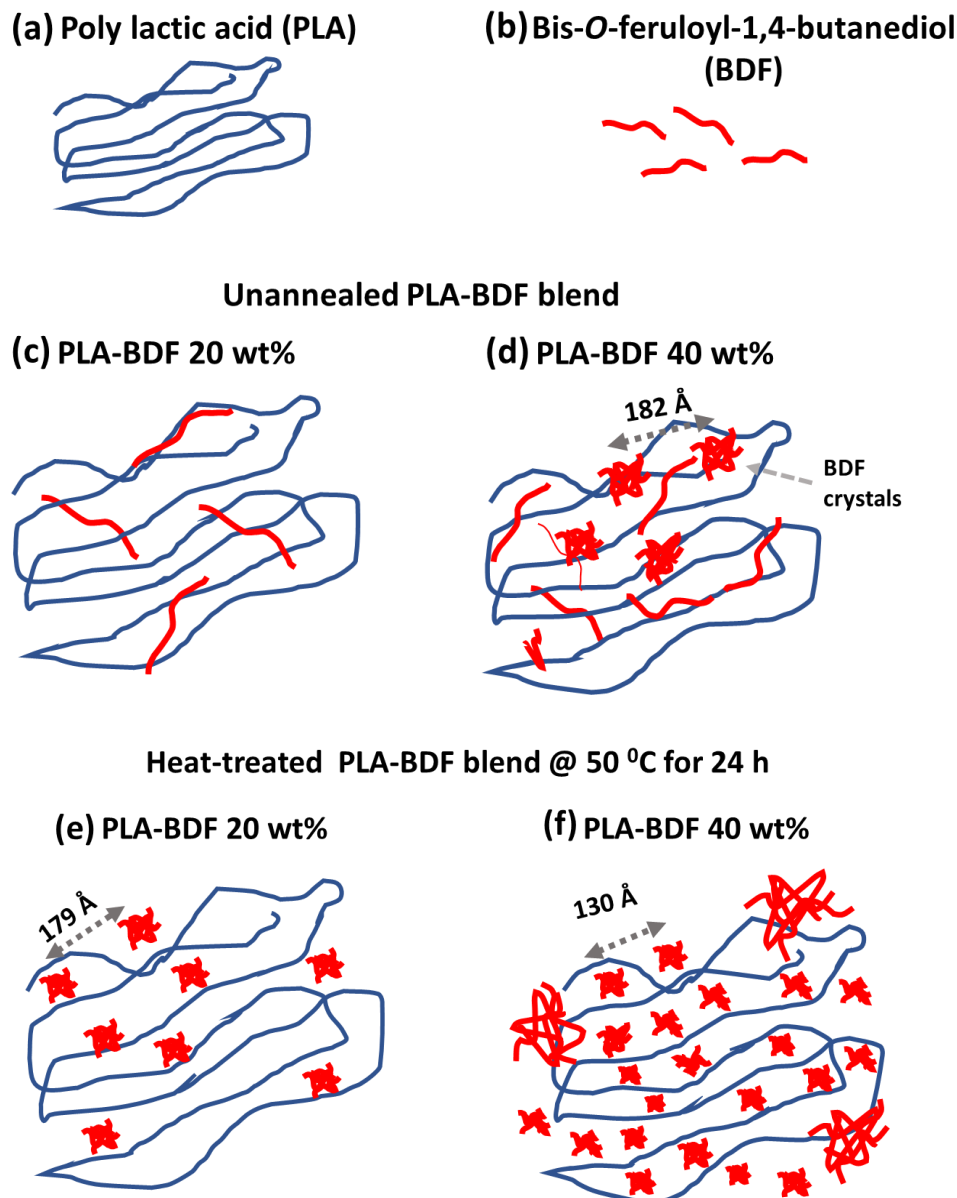

Figure 9: Schematic structure representation of the PLA (a), BDF (b), unannealed blend of PLA-BDF 20 wt% (c), and PLA-BDF 40 wt% (d). Structure of heat-treated blends (50 °C for 24 h) BDF for concentrations of 20 wt% (e) and 40 wt% (f).

Conclusion

The nanocrystallisation of a biosourced additive of Bis-*O*-feruloyl-1,4-butanediol (BDF) blended in PLA is studied at BDF concentrations ranging from 10 to 40 wt %. This is to understand the mechanisms behind the unique elastomeric and transparent properties of the thermoplastic blend which are in sharp contrast with the plastic and brittle nature of PLA. Upon heat-treatment at 50 °C for 24 h, the BDF molecules crystallise in the PLA-BDF blend. Previously, these PLA-BDF blends have shown extraordinary shape memory behaviour[29] and potential as substitute for petro-based and non-biodegradable polymers like polyurethane

and polyether-ether ketone[5, 38]. In this study, pure PLA shows the semicrystalline phase by XRD which remains unchanged upon heat-treatment. The unannealed PLA-BDF- up to a threshold BDF concentration of 20 wt% -reveals homogeneous distribution of the BDF molecules in the PLA network. Here, the BDF molecules are bonded with the PLA network and do not have the sufficient energy to crystallise.

Surprisingly, the unannealed PLA-BDF 40 wt% blend shows BDF crystalline phases by XRD and large structures by SEM. A correlation peak from the SAXS analysis confirms the presence of nanoscale structure assemblies with particle size of 117 Å and interparticle distance of 182 Å. At higher BDF concentrations, the adjacent BDF molecules interact at room temperature, due to low T_g, and form BDF crystals upon aging. The amorphous BDF molecules and crystallised BDF are still bonded with the PLA network, as reflected by the larger interparticle distance, low particle number density and weak interparticle interactions measured.

Heat-treatment of PLA-BDF blends shows BDF crystallisation and phase separated structures in the PLA network. Upon heat treatment, the external heat energy disrupts the PLA-BDF bonds which provides more freedom to the BDF molecules to move, change conformation and interact with other BDF molecules to crystallise. An increase in BDF concentration in the blend decreases the size of the BDF nanocrystals which are brought closer together by stronger interparticle interaction, contributing to a higher number density. This new understanding of the crystallisation mechanisms of the novel biosourced BDF additives in PLA networks will help to efficiently engineer PLA technology for specific elastomeric applications as 3D printing, body implants, smart medical devices and sensors.

Conflicts of interest
There are no conflicts of interest to declare.

Acknowledgement

References

[1] Y. Ramot, M. Haim-Zada, A.J. Domb, A. Nyska, Biocompatibility and safety of PLA and its copolymers, Advanced Drug Delivery Reviews 107 (2016) 153-162.
[2] J.M. Zuidema, A. Bertucci, J. Kang, M.J. Sailor, F. Ricci, Hybrid polymer/porous silicon nanofibers for loading and sustained release of synthetic DNA-based responsive devices, Nanoscale 12(4) (2020) 2333-2339.
[3] K. Rathi, K. Pal, Wireless Hand-Held Device Based on Polylactic Acid-Protected, Highly Stable, CTAB-Functionalized Phosphorene for CO2 Gas Sensing, ACS Applied Materials & Interfaces 12(34) (2020) 38365-38375.
[4] V. Nagarajan, A.K. Mohanty, M. Misratt, Perspective on Polylactic Acid (PLA) based Sustainable Materials for Durable Applications: Focus on Toughness and Heat Resistance, Acs Sustain Chem Eng 4(6) (2016) 2899-2916.

[5] S.M. Lai, Y.C. Lan, Shape memory properties of melt-blended polylactic acid (PLA)/thermoplastic polyurethane (TPU) bio-based blends, J Polym Res 20(5) (2013).

[6] A. Siahsarani, A.H. Behravesh, M. Barmouz, Compressive shape memory behavior of spring-shaped polylactic acid alloy type, J Appl Polym Sci 134(30) (2017).

[7] E.L. Papadopoulou, U.C. Paul, T.N. Tran, G. Suarato, L. Ceseracciu, S. Marras, R. d'Arcy, A. Athanassiou, Sustainable Active Food Packaging from Poly(lactic acid) and Cocoa Bean Shells, ACS Applied Materials & Interfaces 11(34) (2019) 31317-31327.

[8] M. Atreya, K. Dikshit, G. Marinick, J. Nielson, C. Bruns, G.L. Whiting, Poly(lactic acid)-Based Ink for Biodegradable Printed Electronics With Conductivity Enhanced through Solvent Aging, ACS Applied Materials & Interfaces 12(20) (2020) 23494-23501.

[9] Y. Wang, C. Li, T. Wang, X. Li, X. Li, Polylactic Acid–Graphene Oxide-based Materials for Loading and Sustained Release of Poorly Soluble Pesticides, Langmuir 36(41) (2020) 12336-12345.

[10] R. Arjmandi, A. Hassan, Z. Zakaria, Polylactic Acid Green Nanocomposites for Automotive Applications, in: M. Jawaid, M.S. Salit, O.Y. Alothman (Eds.), Green Biocomposites: Design and Applications, Springer International Publishing, Cham, 2017, pp. 193-208.

[11] Y.-H. Jiao, Y. Li, S. Wang, K. Zhang, Y.-G. Jia, Y. Fu, Layer-by-Layer Assembly of Poly(lactic acid) Nanoparticles: A Facile Way to Fabricate Films for Model Drug Delivery, Langmuir 26(11) (2010) 8270-8273.

[12] S. Sato, T. Nyuui, G. Matsuba, K. Nagai, Correlation Between Interlamellar Amorphous Structure and Gas Permeability in Poly(lactic acid) Films, J Appl Polym Sci 131(16) (2014).

[13] M. Jamshidian, E. Arab-Tehrany, M. Imran, M. Jacquot, S. Desobry, Poly-Lactic Acid: Production, Applications, Nanocomposites, and Release Studies, Comprehensive Reviews in Food Science and Food Safety 9 (2010) 552-571.

[14] J.H. Kim, H. Noh, J.H. Kang, B.S. Lee, J. Choi, K. Park, D.K. Han, Characteristics of PLLA films blended with PEG block copolymers as additives for biodegradable polymer stents, Biomedical Engineering Letters 1(1) (2011) 42-48.

[15] R. Bhardwaj, A.K. Mohanty, Modification of Brittle Polylactide by Novel Hyperbranched Polymer-Based Nanostructures, Biomacromolecules 8(8) (2007) 2476-2484.

[16] Y. Sun, C. He, Biodegradable "Core–Shell" Rubber Nanoparticles and Their Toughening of Poly(lactides), Macromolecules 46(24) (2013) 9625-9633.

[17] J.-F. Ru, S.-G. Yang, J. Lei, Z.-M. Li, Thicker Lamellae and Higher Crystallinity of Poly(lactic acid) via Applying Shear Flow and Pressure and Adding Poly(ethylene Glycol), The Journal of Physical Chemistry B 121(23) (2017) 5842-5852.

[18] H. Fang, F. Jiang, Q. Wu, Y. Ding, Z. Wang, Supertough Polylactide Materials Prepared through In Situ Reactive Blending with PEG-Based Diacrylate Monomer, ACS Applied Materials & Interfaces 6(16) (2014) 13552-13563.

[19] L.V. Labrecque, R.A. Kumar, V. Davé, R.A. Gross, S.P. McCarthy, Citrate esters as plasticizers for poly(lactic acid), Journal of Applied Polymer Science 66(8) (1997) 1507-1513.

[20] J.-B. Zeng, Y.-D. Li, Y.-S. He, S.-L. Li, Y.-Z. Wang, Improving Flexibility of Poly(l-lactide) by Blending with Poly(l-lactic acid) Based Poly(ester-urethane): Morphology, Mechanical Properties, and Crystallization Behaviors, Industrial & Engineering Chemistry Research 50(10) (2011) 6124-6131.

[21] M.-B. Coltelli, I.D. Maggiore, M. Bertoldo, F. Signori, S. Bronco, F. Ciardelli, Poly(lactic acid) properties as a consequence of poly(butylene adipate-co-terephthalate) blending and acetyl tributyl citrate plasticization, Journal of Applied Polymer Science 110(2) (2008) 1250-1262.

[22] J. Yu, N. Wang, X. Ma, Fabrication and Characterization of Poly(lactic acid)/Acetyl Tributyl Citrate/Carbon Black as Conductive Polymer Composites, Biomacromolecules 9(3) (2008) 1050-1057.

[23] K. Zhang, V. Nagarajan, M. Misra, A.K. Mohanty, Supertoughened Renewable PLA Reactive Multiphase Blends System: Phase Morphology and Performance, ACS Applied Materials & Interfaces 6(15) (2014) 12436-12448.

[24] L. Jiang, M.P. Wolcott, J. Zhang, Study of Biodegradable Polylactide/Poly(butylene adipate-co-terephthalate) Blends, Biomacromolecules 7(1) (2006) 199-207.

[25] M.A. Shirai, M.V.E. Grossmann, S. Mali, F. Yamashita, P.S. Garcia, C.M.O. Müller, Development of biodegradable flexible films of starch and poly(lactic acid) plasticized with adipate or citrate esters, Carbohydrate Polymers 92(1) (2013) 19-22.

[26] O. Martin, L. Averous, Poly(lactic acid): plasticization and properties of biodegradable multiphase systems, Polymer 42(14) (2001) 6209-6219.

[27] K.Y. Zhang, X.H. Ran, X.M. Wang, C.Y. Han, L.J. Han, X. Wen, Y.G. Zhuang, L.S. Dong, Improvement in Toughness and Crystallization of Poly(L-lactic acid) by Melt Blending with Poly(epichlorohydrin-co-ethylene oxide), Polym Eng Sci 51(12) (2011) 2370-2380.

[28] H. Liu, J. Zhang, Research progress in toughening modification of poly(lactic acid), Journal of Polymer Science Part B: Polymer Physics 49(15) (2011) 1051-1083.

[29] A. Gallos, J.-M. Crowet, L. Michely, V.S. Raghuwanshi, M.M. Mention, V. Langlois, M. Dauchez, G. Garnier, F. Allais, Blending Ferulic Acid Derivatives and Polylactic Acid into Biobased and Transparent Elastomeric Materials with Shape Memory Properties, Biomacromolecules (2021).

[30] B.A. Bruker, TOPAS V4: General profile and structure analysis software for powder diffraction data. - User's Manual, Bruker AXS, Karlsruhe, Germany, 2008.

[31] N.M. Kirby, S.T. Mudie, A.M. Hawley, D.J. Cookson, H.D.T. Mertens, N. Cowieson, V. Samardzic-Boban, A low-background-intensity focusing small-angle X-ray scattering undulator beamline, J Appl Crystallogr 46 (2013) 1670-1680.

[32] I. Bressler, B.R. Pauw, A.F. Thunemann, McSAS: software for the retrieval of model parameter distributions from scattering patterns, J Appl Crystallogr 48 (2015) 962-969.

[33] B.D.C. Cullity, Elements of X-ray Diffraction, ADDISON-WESLEY PUBLISHING COMPANY INC, USA, 1978.

[34] O.a.K. Glatter, O., Small-angle X-ray Scattering, Academic Press, London.1982.

[35] V.S. Raghuwanshi, U.M. Garusinghe, P. Raj, N. Kirby, A. Hoell, W. Batchelor, G. Garnier, Cationic polyacrylamide induced nanoparticles assembly in a cellulose nanofiber network, J Colloid Interf Sci 529 (2018) 180-186.

[36] V.S. Raghuwanshi, U.M. Garusinghe, J. Ilaysky, W.J. Batchelor, G. Gamier, Effect of nanoparticles size and polyelectrolyte on nanoparticles aggregation in a cellulose fibrous matrix, J Colloid Interf Sci 510 (2018) 190-198.

[37] V.S. Raghuwanshi, M. Ochmann, F. Polzer, A. Hoell, K. Rademann, Self-assembly of gold nanoparticles on deep eutectic solvent (DES) surfaces, Chem Commun 50(63) (2014) 8693-8696.

[38] L. Zhang, Z.H. Lin, Q. Zhou, S.Q. Ma, Y.H. Liang, Z.H. Zhang, PEEK modified PLA shape memory blends: towards enhanced mechanical and deformation properties, Front Mater Sci 14(2) (2020) 177-187.

[A]Casalini T, Rossi F, Castrovinci A and Perale G (2019) A Perspective on Polylactic Acid-Based Polymers Use for Nanoparticles Synthesis and Applications. Front. Bioeng. Biotechnol. Vol 7 (2019) article 259. doi: 10.3389/fbioe.2019.00259.

[B] Improvements and considerations for size distribution retrieval from small-angle scattering data by Monte Carlo methods. Pauw BR, Pedersen JS, Tardif S, Takata M, Iversen BB, J Appl Crystallogr. 2013 Apr 1; 46(Pt 2):365-371.

[C] I. Bressler, B. R. Pauw, and A. F. Thünemann, McSAS: software for the retrieval of model parameter distributions from scattering pattern, J Appl Crystallogr. 2015; 48(Pt 3): 962–969.